Biochemical and Biophysical Research Communications 738 (2024) 150544

Contents lists available at ScienceDirect

Biochemical and Biophysical Research Communications

journal homepage: www.elsevier.com/locate/ybbrc

# Cryo-EM structure of the human glucose transporter GLUT7

Sang Soo Lee, Subin Kim, Mi Sun Jin *

*School of Life Sciences, GIST, 123 Cheomdangwagi-ro, Buk-gu, Gwangju, 61005, Republic of Korea*

ARTICLE INFO

*Keywords:*
Human glucose transporter 7
SLC2A7
Fructose transporter
Intestinal hexose absorption
Substrate translocation
Sugar transporter

ABSTRACT

GLUT7 is a Class II glucose transporter predominantly expressed at the apical membrane of enterocytes in the small intestine. Here, we report the cryo-EM structure of nanodisc-reconstituted human GLUT7 in the apo state at 3.3 Å resolution. Our atomic model reveals a typical major facilitator superfamily fold, with the substrate-binding site open to the extracellular side of the membrane. Despite the nearly identical conformation to its closest family member, rat GLUT5, our structure unveils distinct features of the substrate-binding cavity that may influence substrate specificity and binding mode. A homology model of the inward-open human GLUT7 indicates that similar to other members of the GLUT family, it may undergo a global rocker-switch-like reorientation of the transmembrane bundles to facilitate substrate translocation across the membrane. Our work enhances the current structural understanding of the GLUT family, and lays a foundation for rational design of regulators of GLUTs and other sugar transporters.

## 1. Introduction

Solute Carrier (SLC) 2 genes encode a family of glucose transporters (GLUTs) belonging to the major facilitator superfamily (MFS) of membrane transporters [1,2]. These proteins play a critical role in cellular energy homeostasis by facilitating the transport of glucose and other hexoses across the cellular membrane. Their dysfunction or misregulation is known to underlie clinical problems such as type 2 diabetes and certain types of cancer [3,4]. To date, 14 GLUT proteins have been identified, and they are categorized into three phylogenetically distinct classes based on sequence similarity: Class I (GLUTs 1−4 and 14), Class II (GLUTs 5, 7, 9, and 11), and Class III (GLUTs 6, 8, 10, 12, and 13) [5]. Class I GLUTs primarily transport glucose transport, but this is not necessarily the case for Class II and III transporters. For instance, GLUT9 functions as a urate transporter, playing a role in uric acid homeostasis [6]. GLUT13, also known as HMIT, is expressed predominantly in neuronal tissues [7] and is unique among GLUT proteins in functioning as a proton-coupled myo-inositol transporter [8]. This diversity in substrate specificity and function highlights the complexity of GLUTs and their varied roles in cellular metabolism.

Class II GLUTs have attracted considerable attention due to their preferential transport of fructose over glucose. GLUT5, for example, is expressed in the small intestine, kidney, and sperm, and is highly regulated in response to fructose levels [9,10]. GLUT7 shares ~50 % sequence identity with GLUT5 and is predominantly expressed in the small intestine, colon, testis, and prostate [11]. Despite initial reports suggesting that GLUT7 functions as a high-affinity, low-capacity fructose transporter based on studies in *Xenopus* oocytes [12,13], more recent studies have demonstrated negligible fructose transport by GLUT7 in mammalian cells compared with GLUT5 [14]. Moreover, chimeric studies introducing GLUT7 domains into GLUT5 produced functionally inactive proteins, indicating that GLUT7 might have different substrates or functions [15]. These findings underscore the need for a deeper structural and functional understanding of GLUT7.

GLUT proteins share a common architecture, featuring 12 transmembrane helices (TMs) with both N- and C-termini located intracellularly [16]. The structures of GLUTs have been studied extensively by X-ray crystallography and cryo-electron microscopy (cryo-EM), providing significant insights into their conformational dynamics during the transport cycle [17–21]. For instance, the structure of human GLUT1 bound to nonyl-β-D-glucoside revealed a central cavity open to the intracellular side, with the extracellular cavity completely blocked off [17]. Its bacterial homolog, the *Escherichia coli* XylE, displayed an inward-occluded conformation when in complex with a substrate or inhibitor [22]. By contrast, the structure of human GLUT3 with exofacially bound maltose or glucose adopted outward-open and outward-occluded states, respectively [18]. These findings strongly support the 'rocker-switch'-type alternating access hypothesis, involving cyclic transitions between inward- and outward-facing conformational states essential for substrate translocation.

* Corresponding author.
*E-mail address:* misunjin@gist.ac.kr (M.S. Jin).

https://doi.org/10.1016/j.bbrc.2024.150544
Received 7 August 2024; Received in revised form 8 August 2024; Accepted 12 August 2024
Available online 13 August 2024
0006-291X/© 2024 The Authors. Published by Elsevier Inc. This is an open access article under the CC BY license (http://creativecommons.org/licenses/by/4.0/).

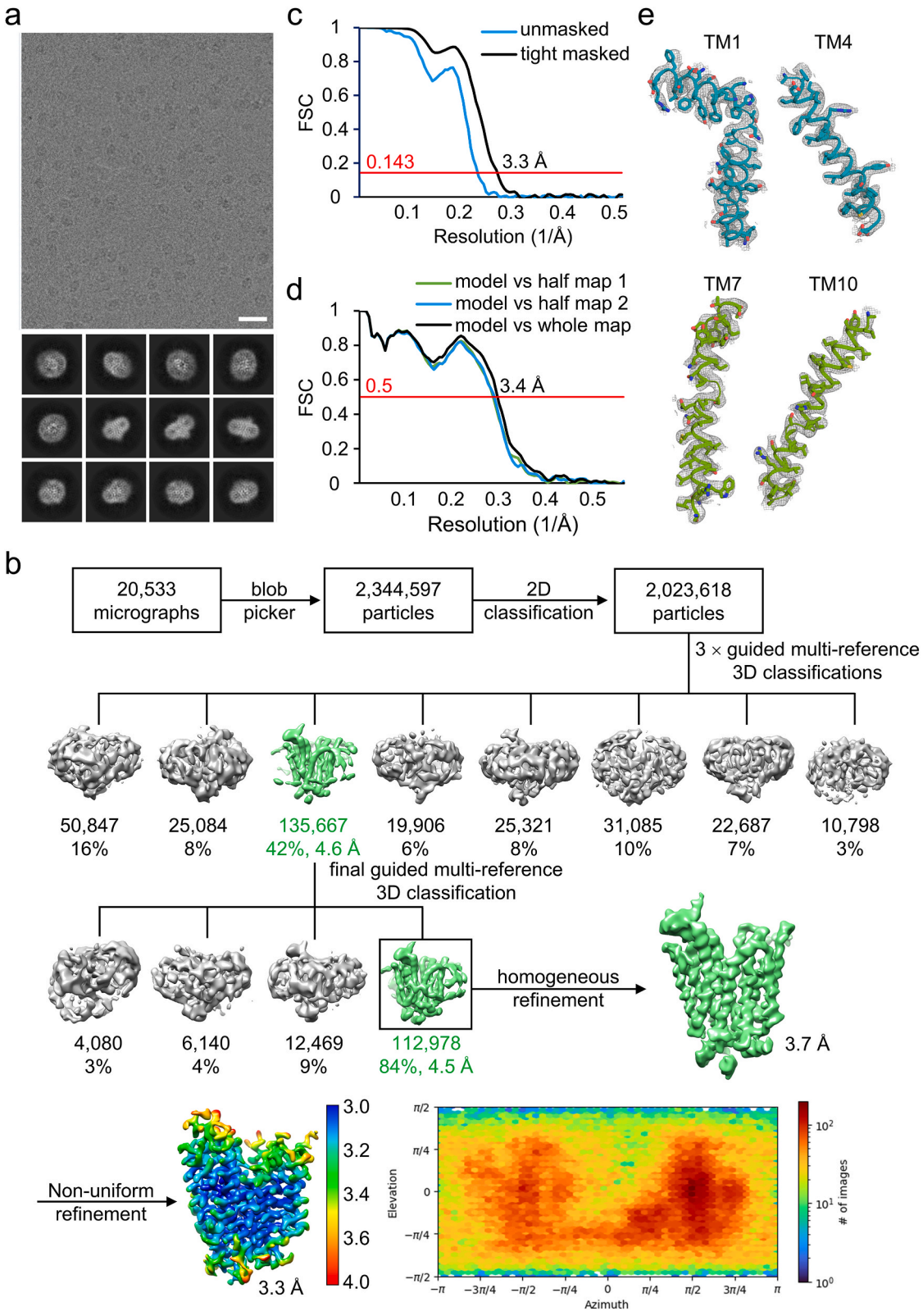


**Fig. 1. Cryo-EM structure determination of human GLUT7.** (a) Representative micrograph (upper panel, scale-bar-200 Å) and 2D class averages (lower panel). (b) Flowchart for EM data processing and angular distribution curve for the final refinement (lower right panel). (c) Gold-standard Fourier shell correlation (FSC) curves calculated from two independently refined half-maps. The red line represents the FSC criterion of 0.143. (d) FSC curves calculated between the refined structure and the half map used for refinement (green), the other half map (blue), and the summed map (black). The red line represents the 0.5 FSC cutoff criterion. (e) EM maps for representative TM helices contoured at 4 σ. (For interpretation of the references to colour in this figure legend, the reader is referred to the Web version of this article.)

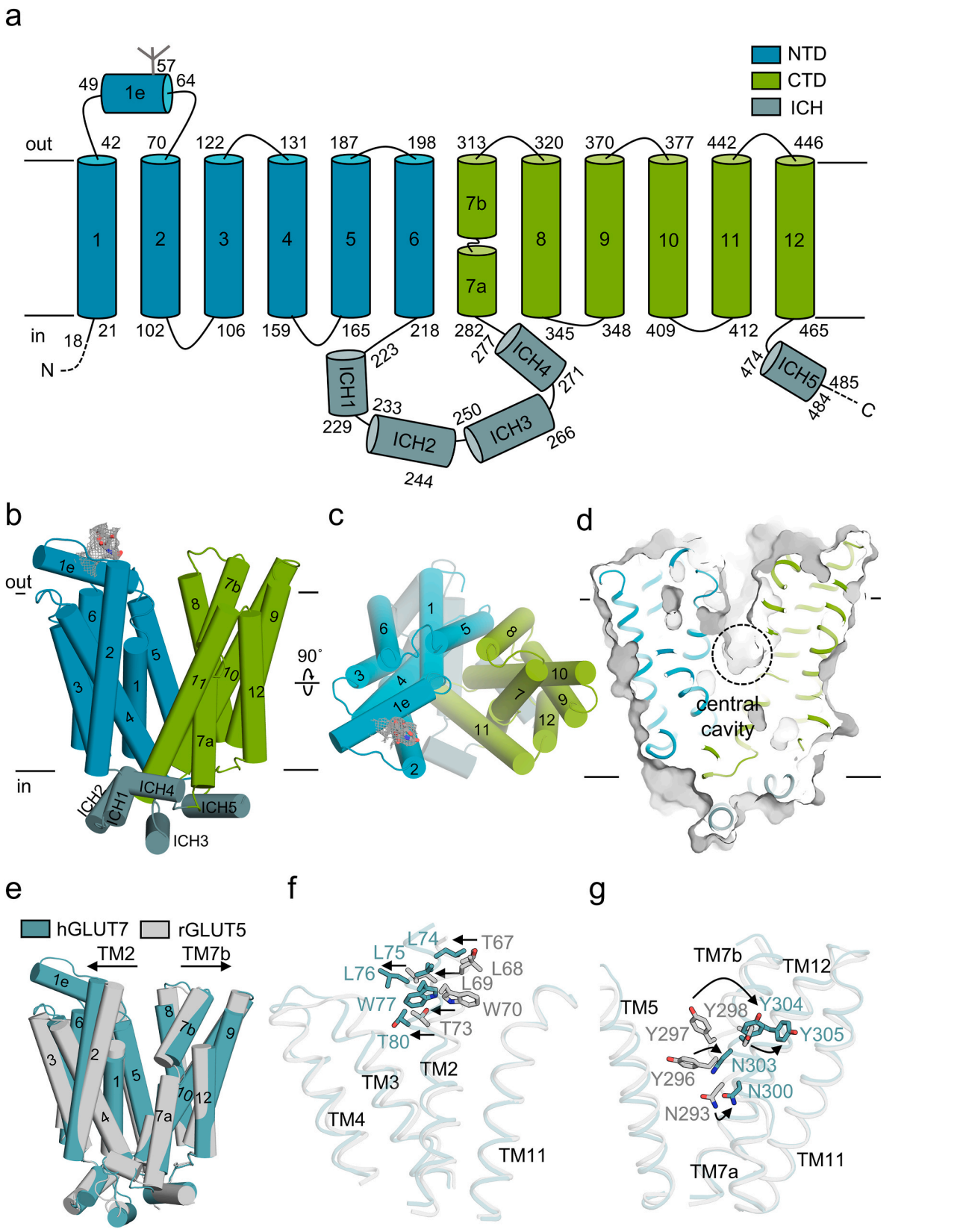


**Fig. 2. Outward-open structure of human GLUT7.** (a) Topology of human GLUT7. The N-linked glycosylation site is indicated at N57. Dotted lines indicate regions that were not modeled in the final EM map. (b, c) Cryo-EM structure of GLUT7 in an outward-open state. The density for the N-glycan attached to N57 is contoured at 4 σ. (d) Slab view of GLUT7. (e) Structure of rat GLUT5 (PDB code 4YBQ) overlaid onto the structure of human GLUT7. TM11 is omitted for a clear view of the movement of TM7b. (f, g) Local conformational shifts of TM 2 (f) and TM 7b (g) that widen the path to the central pocket.

In this work, we present the cryo-EM structure of human GLUT7 in lipid nanodiscs at 3.3 Å resolution, providing a detailed description of its apo and outward-open state. Combined with a homology model of GLUT7 in the inward-open conformation, our findings shed light on its possible mechanism of substrate transport across the membrane. These insights have the potential for advancing research into GLUT-associated diseases and the development of targeted therapeutics.

## 2. Materials and methods

### 2.1. Cloning, expression, and purification

The gene encoding the full-length human GLUT7 was codon-optimized (Gene Universal) and cloned into pVL1393 (BD Biosciences) with a thrombin-cleavable enhanced green fluorescence protein (eGFP) and decahistidine (His10) affinity tag at the C-terminus. Recombinant baculoviruses were generated in *Spodoptera frugiperda* Sf9 cells using the BestBac 2.0 baculovirus expression system (Expression Systems). High five (Hi5) cells were cultured at 28 °C for 72 h following infection, then harvested by centrifugation at 7700 g for 10 min. The cell pellet was resuspended in lysis buffer containing 20 mM HEPES-NaOH pH 7.0, 200 mM NaCl, 1 mM phenylmethylsulfonyl fluoride (PMSF), and 40 μg/mL DNase I.

All purification steps were performed on ice or at 4 °C. Cell membranes were disrupted by sonication for 3 min, then subjected to ultracentrifugation at 300,000 g for 1 h. The resulting membrane pellet was resuspended in lysis buffer and solubilized in 2 % (w/v) *n*-dodecyl-β-D-maltopyranoside (DDM; Anatrace) and 0.2 % (w/v) cholesteryl hemisuccinate (CHS; Anatrace) for 2 h with gentle stirring. Insoluble cell debris was removed by ultracentrifugation at 300,000 g for 1 h and the supernatant was loaded onto anti-GFP DARPin resin [23]. After washing the resin with buffer containing 20 mM HEPES-NaOH pH 7.0, 200 mM NaCl, 0.0174 % (w/v) DDM, and 0.00174 % (w/v) CHS, the protein was eluted by on-column thrombin cleavage (Lee Biosolutions). Protein was further purified by gel filtration chromatography using a Superdex 200 Increase 10/300 GL column (Cytiva) equilibrated with DDM buffer.

### 2.2. Nanodisc reconstruction

The gene encoding membrane scaffold protein MSP1D1, a synthetic derivative of apolipoprotein A-I, was expressed and purified as previously described [24,25]. Porcine brain polar lipid extract (Avanti Polar Lipids) were utilized for nanodisc assembly. Chloroform in the lipid solution was evaporated using a gentle stream of nitrogen gas to form a thin lipid film. This lipid film was subsequently dissolved in buffer consisting of 20 mM HEPES-NaOH pH 7.0, 200 mM NaCl, 0.0174 % (w/v) DDM, and 0.00174 % (w/v) CHS. After sonication in a water bath at 22 °C for 1 min, the lipid solution was mixed with MSP1D1 and GLUT7 at a molar ratio of 150:5:1 and incubated at 4 °C for 2 h. To remove detergent, the mixture was treated with SM2 Bio-Beads (Bio-Rad). Finally, the supernatant was subjected to a Superdex 200 Increase 10/300 GL column equilibrated with dissolving buffer lacking detergent and CHS. This step was performed to isolate the protein-loaded nanodiscs while removing any empty nanodiscs and unloaded proteins.

### 2.3. Grid preparation and data acquisition

The sample (3 μL at 1 mg/mL) was applied onto a freshly glow-discharged Quantifoil holey carbon grid (R1.2/1.3, Au, 300 mesh). The grids were blotted for 3 s at 4 °C in 100 % humidity and plunge-frozen in liquid ethane using a Vitrobot Mark IV instrument (Thermo Fisher Scientific). Cryo-EM imaging was performed on a 300 kV Titan Krios G4 microscope equipped with a cold-FEG, a Falcon 4i direct electron detector, and a Selectris X energy filter (Thermo Fisher Scientific). A total of 20,533 micrographs was collected using EPU software in the electron counting mode at a pixel size of 0.57 Å (magnification 215,000 × ) and a defocus range from −0.6 to −2.2 μm. The total exposure time was 2.46 s and each movie was fractionated into 50 frames with a total dose of 50 $e^-/Å^2$. The electron dose rate was 7.14 $e^-$/pix/s (1 $e^-/Å^2$/frame). The detailed cryo-EM data collection parameters are summarized in Supplemental Table 1.

### 2.4. Electron microscopy data processing

All image processing was carried out in cryoSPARC 4.1.2 [26]. Micrographs were initially motion-corrected using patch motion correction, and contrast transfer function (CTF) parameters were determined using patch CTF estimation. Particles were picked using reference-free blob picker, followed by particle extraction with a box size of 300 pixels. After 2D classification, 2,023,618 particles were chosen for *ab initio* reconstruction. Four subsequent rounds of heterogeneous refinement were performed to classify particles and volumes showing transmembrane helices. Ultimately, a set of 112,978 particles of the best-resolved class was selected for further homogeneous and non-uniform refinement [27], yielding a density map at a resolution of 3.3 Å. The detailed data processing pipeline is shown in Fig. 1.

### 2.5. Model building and refinement

The structural model of human GLUT7 was built based on an initial model predicted by AlphaFold2 [28]. This model was roughly fitted into the EM density map using UCSF Chimera [29] and subsequently subjected to multiple rounds of real space refinement with secondary structure and geometry restraints in PHENIX [30]. Coot was used to manually fit coordinates into the EM density [31]. The final structure was validated by MolProbity [32]. Structural figures were prepared using PyMOL (https://pymol.org). Model refinement and validation statistics are summarized in Supplementary Table 1.

## 3. Results and discussion

### 3.1. Structure determination

For a single-particle cryo-EM analysis of human GLUT7 in the apo state, full-length protein was expressed using a baculovirus insect cell expression system and reconstituted into nanodiscs, resulting in well-dispersed particles when imaged on a 300 kV Titan Krios microscope (Fig. 1a, top). The 2D class averages revealed various views of particles with structural features of TM helices within a lipid envelope (Fig. 1a, bottom). However, the relatively small size (55 kDa) without symmetry and lack of a stable soluble domain made data processing challenging. To overcome these technical barriers, we applied four rounds of three-dimensional (3D) heterogeneous refinement using a “guided multi-reference 3D classification strategy” [33]. This method has been proven effective in determining cryo-EM structures of small size membrane proteins by eliminating strong noise and identifying high-quality particles (Fig. 1b) [21,33]. In the final 3D heterogeneous refinement, 112,978 high-quality particles converged into the best class containing 84 % of input particles, yielding an average resolution of 4.5 Å. These overall resolution was further improved to 3.3 Å by 3D homogeneous refinement and non-uniform refinement (Fig. 1b–d) [27]. The final EM map allowed for assignment of 468 amino acids in the 12 TM helices and the intracellular helical (ICH) domain, with the exception of the extreme N- and C-termini (Fig. 1e and Fig. 2a.).

### 3.2. Overall fold

Human GLUT7 adopts a typical MFS fold with the central substrate-binding cavity enclosed within the N-terminal domain (NTD) comprising TM helices 1–6 and the C-terminal domain (CTD) comprising TM helices 7–12 (Fig. 2a–d). Due to its discontinuity, TM7 was designated TM7a/7b. The N-terminal and C-terminal TM bundles

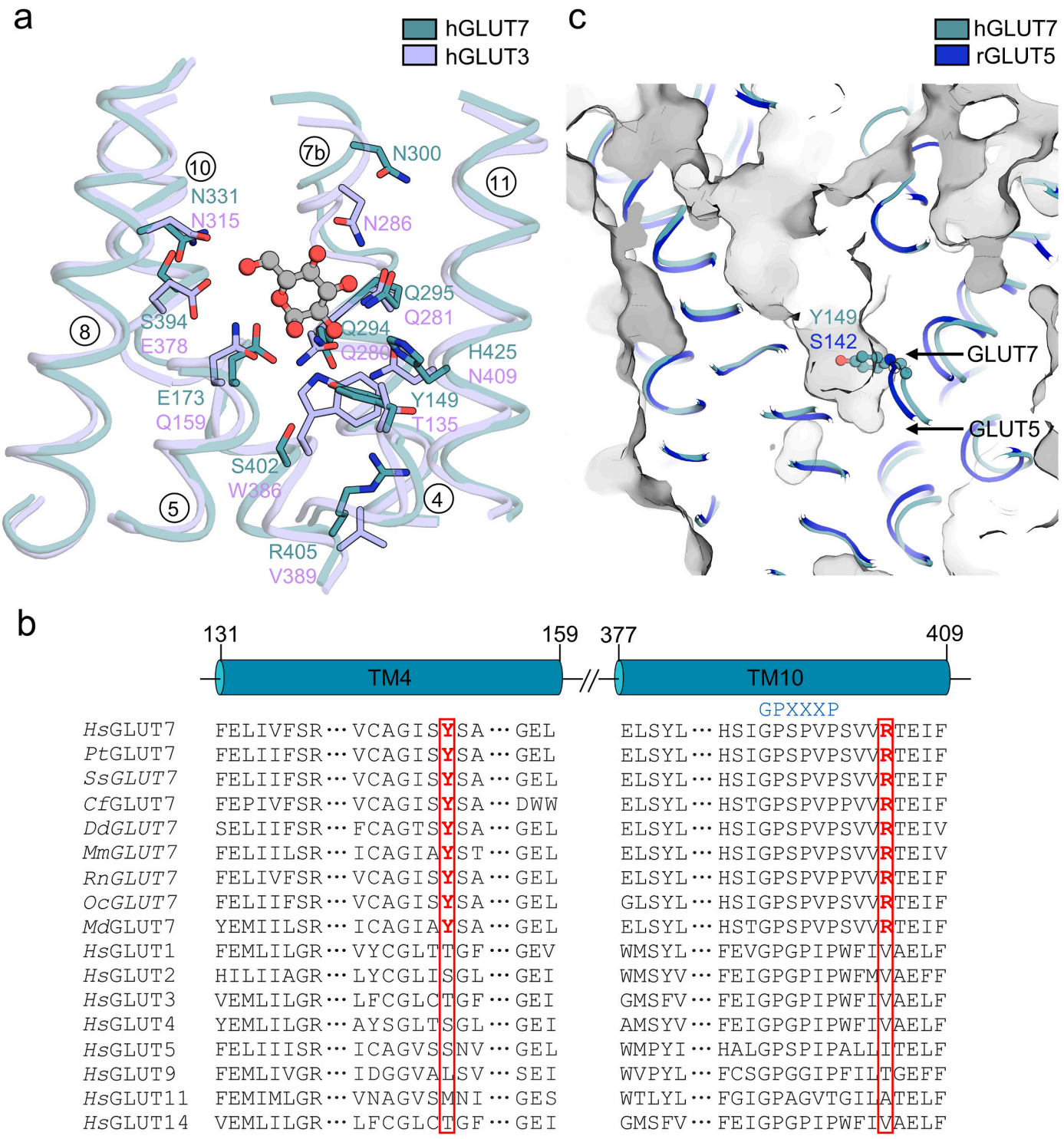


**Fig. 3. Substrate-binding cavity.** (a) Superimposition of the substrate-binding sites of human GLUT3 (PDB code 4ZW9) and human GLUT7. Residues involved in glucose binding in GLUT3 (purple) and their equivalents in GLUT7 (teal) are shown as sticks. (b) Amino acid sequence alignments of GLUT7 homologs. The strictly conserved "tyrosine-arginine" pair is highlighted in red. A schematic representation of the secondary structural elements and the conserved GPXXXP motif is displayed above the sequences. *Hs, Homo sapiens; Pt, Pan troglodytes; Ss, Sus scrofa; Cf, Camelus ferus; Dd, Delphinus delphis; Mm, Mus musculus; Rn, Rattus norvegicus; Oc, Oryctolagus cuniculus; Md, Malus domestica.* (c) Slab view of the central cavity of rat GLUT5 (PDB code 4YBQ, gray/blue) with the superimposed human GLUT7 structure (teal). Y149 in GLUT7 is replaced by serine (S142) in GLUT5, resulting in a deeper cavity. The arrows point to the bottom of each cavity. (For interpretation of the references to colour in this figure legend, the reader is referred to the Web version of this article.)

are related by a pseudo-two-fold symmetry axis parallel to the membrane, with each domain comprising '3 + 3′ inverted repeats [34]. Five ICHs are also clearly visible in the cryo-EM map: four helices (ICH1–ICH4) between TM6 and TM7, and one at the C-terminus (ICH5). In the cryo-EM map, the glycan density is observed in N57 (Fig. 2a–c). The substrate-binding cavity is located halfway across the membrane height and is exposed towards the extracellular side (Fig. 2d). GLUT5, which is most closely related to GLUT7, was recently crystallized in the

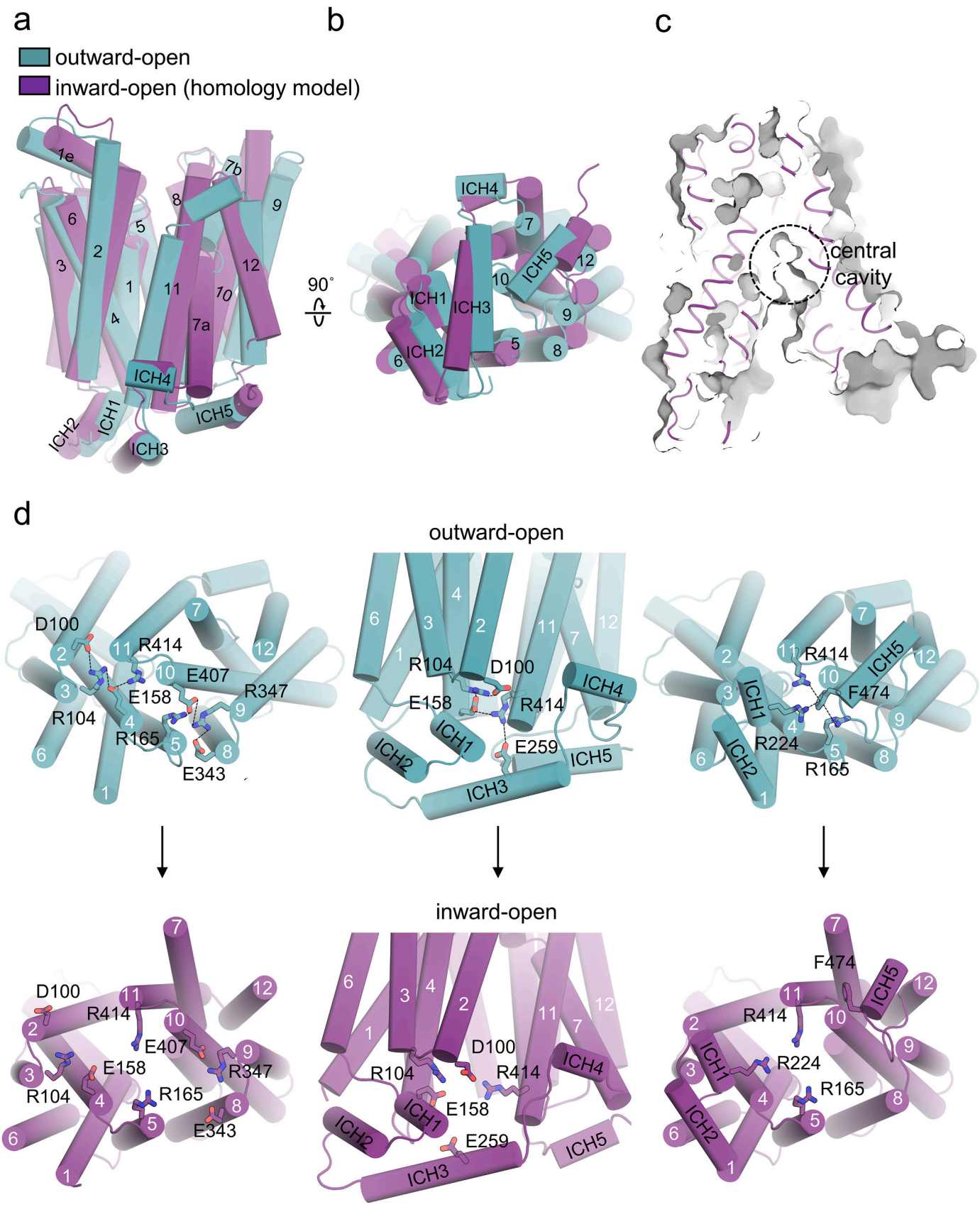


**Fig. 4. Possible mechanism of the conformational transition.** (a, b) Superimposition of the outward-open (teal) and inward-open (violet) homology model of human GLUT7. (c) Slab view of the inward-open homology model. (d) Conformational changes of the TM bundles and ICH domains between the outward-open structure (upper panels) and inward-open homology model (bottom panels) of GLUT7. (For interpretation of the references to colour in this figure legend, the reader is referred to the Web version of this article.)

absence of the substrate fructose in an inward-open conformation (bovine) and an outward-open conformation (rat) [19]. Although human GLUT7 and rat GLUT5 share only 57 % sequence identity, their outward-facing structures superimpose well, with a Cα root mean square deviation of 1.4 Å (Fig. 2e). However, structural comparison demonstrated that TM2 and TM7b undergo the most extensive local shifts, moving away from the central pathway. These changes result in the repositioning of residues, particularly the bulky resides W77 (TM2), Y304, and Y305 (TM7b), causing them to point away from the transport pathway (Fig. 2f and g). Consequently, the extracellular vestibule of GLUT7 is wider than that of rat GLUT5, which likely enhances substrate access to the central cavity.

### 3.3. Substrate-binding cavity

Despite controversy over its correct physiological substrate, GLUT7 has been reported to transport both fructose and glucose [11]. Since the rat GLUT5 structure was determined without a bound substrate [19], we aligned the human GLUT7 structure with human GLUT3 in complex with glucose to gain insights into the substrate-binding site of GLUT7 [18]. Superimposition of the two proteins indicates that the potential substrate-coordinating residues of GLUT7 include E173, Q294, Q295, N331, H425, Y149, and S402 (Fig. 3a). In GLUT3, N286 is also involved in substrate binding, whereas the corresponding residue in GLUT7 (N300) is somewhat distant from the central cavity. However, as observed in other GLUTs [18,35], substrate binding likely induces GLUT7 occlusion by causing TM7b to tilt towards the transport pathway, which allows N300 to engage in substrate coordination. Among the residues lining the central cavity, the most notable difference is the replacement of the tryptophan residue at the bottom of the cavity in GLUT3 (W386), which is essential in the recognition of sugars or inhibitors for Class I GLUTs, with serine (S402) in GLUT7 [18,22,35–37]. This structural feature is consistent with protein sequence analysis, which indicates that Class II GLUTs lack the tryptophan residue following the GPXXXP motif (Fig. 3b) [38]. Another notable difference is the substitution of threonine (T135) in GLUT3 with tyrosine (Y149) in GLUT7 (Fig. 3a). While R405 does not directly participate in substrate binding, it stabilizes the conformation of Y149 through cation-π interactions, orienting it toward the central cavity. This positioning may allow Y149 to participate in substrate binding and/or form a major part of the intracellular gate. In GLUT5, serine (S142) takes the place of Y149, resulting in a deeper cavity than in GLUT7 (Fig. 3c). Sequence alignment reveals that this “tyrosine-arginine” pair is unique to GLUT7, as it is strictly conserved among its homologs, but not present in other GLUTs (Fig. 3b). Additionally, Q159 in GLUT3, a polar residue from the NTD involved in hydrogen bonding with glucose, is replaced by glutamate (E173) in GLUT7 (Fig. 3a) [18]. It is noteworthy that substituting the equivalent glutamine with glutamate (Q166E) in rat GLUT5 weakens fructose binding but maintains robust binding to glucose [18]. Together, these distinctive features of substrate-binding site likely influence the substrate preference of GLUT7.

### 3.4. Alternating access cycle

To gain insights into the molecular basis of the transport mechanism of GLUT7, we constructed a reliable homology model of its inward-open state using the program MODELLER [39]. The model was built using the inward-facing structure of human GLUT4 as the template [21], as it shares sequence identity of 41 % and similarity of 61 % with GLUT7, and is the only GLUT protein with all five cytosolic ICHs clearly resolved in the EM map. Structural comparison revealed that the NTD and the N-terminal ICH domain (ICH1−4) of GLUT7 remain relatively rigid during conformational changes, while the CTD and ICH5 undergo significant rearrangement (Fig. 4a and b). Moreover, the homology model showed that the substrate-binding cavity is solvent-accessible only to the intracellular side of the membrane bilayer (Fig. 4c). The analysis also revealed that key interactions responsible for conformational stability are highly conserved among GLUTs [18,19,21]. For example, in the outward-open conformation, a network of salt bridges is formed between the cytoplasmic ends of TM helices in the NTD and the CTD, with distances <4 Å (Fig. 4d, left). These interactions include D100, E158, R104, and R414 in the NTD region and E407, R165, E343, and R347 in the CTD region. Another salt bridge between E259 and R414 further stabilizes the outward-open conformation of GLUT7 by linking ICH3 to the cytoplasmic ends of TM11 (Fig. 4d, center). By contrast, the homology model indicates that in the inward-facing conformation, these salt-bridge networks are broken, leading to the central cavity opening to the cytoplasm. This analysis is consistent with data showing that disrupting the equivalent salt-bridge network in human GLUT4 locks the transporter in an inward-facing conformation [40]. The ICH5 domain also undergoes significant conformational changes during the transport cycle. In the outward-open state, ICH5 secures the NTD and CTD on the cytoplasm by forming cation-π interactions between F474 on ICH5 and three arginine residues: R165 on TM5, R224 on ICH1, and R414 on TM11 (Fig. 4d, right). These interactions fully dissociate as ICH5 swings outward in the inward-open state. Taken together, our findings suggest that GLUT7 follows the classic “rocker-switch alternating access” model for substrate transport, wherein conformational changes alternately expose its substrate-binding sites on either side of the membrane by rocking the NTD and CTD around a pseudo-2-fold axis [41,42].

In summary, we present the cryo-EM structure of apo human GLUT7 in the outward-open state, offering new insights into the molecular architecture of GLUT proteins, with details of the substrate-binding cavity. We also generated a homology model of GLUT7 in the inward-open conformation, highlighting that key interactions involved in conformational changes are well conserved among GLUT family members. The findings could facilitate the structure-based design of new inhibitors targeting GLUTs with therapeutic potential.

## Data availability

The atomic coordinates of human GLUT7 in the apo, outward-open state have been deposited in the Protein Data Bank under accession code 9J2N. The cryo-EM density map has been deposited in the Electron Microscopy Data Bank under accession code EMD-61099.

## CRediT authorship contribution statement

**Sang Soo Lee:** Visualization, Formal analysis, Data curation, Conceptualization. **Subin Kim:** Visualization, Formal analysis, Data curation, Conceptualization. **Mi Sun Jin:** Writing – review & editing, Writing – original draft, Supervision, Project administration, Funding acquisition, Conceptualization.

## Declaration of competing interest

The authors declare that they have no known competing financial interests or personal relationships that could have appeared to influence the work reported in this paper.

## Acknowledgements

We thank the center for electron microscopy (NanoPort) of Thermo Fisher Scientific in the Netherlands, and the Institute of Membrane Protein (IMP) of POSTECH and the GIST Advanced Institute of Instrumental Analysis (GAIA) of GIST in South Korea for assistance during EM data collection and processing. This research was supported by grants (NRF-2022R1A2C1091278, RS-2024-00344154, and RS-2024-00440614) from the National Research Foundation (NRF) funded by the Korean government (MSIT).

## Appendix A. Supplementary data

Supplementary data to this article can be found online at https://doi.org/10.1016/j.bbrc.2024.150544.

## References


[1] M. Mueckler, B. Thorens, The SLC2 (GLUT) family of membrane transporters, Mol. Aspect. Med. 34 (2013) 121–138, https://doi.org/10.1016/j.mam.2012.07.001.

[2] S.S. Pao, I.T. Paulsen, M.H. Saier Jr., Major facilitator superfamily, Microbiol. Mol. Biol. Rev. 62 (1998) 1–34, https://doi.org/10.1128/MMBR.62.1.1-34.1998.

[3] S.P. Zamora-León, D.W. Golde, I.I. Concha, C.I. Rivas, F. Delgado-Lopez, et al., Expression of the fructose transporter GLUT5 in human breast cancer, Proc. Natl. Acad. Sci. U. S. A. 93 (1996) 1847–1852, https://doi.org/10.1073/pnas.93.5.1847.

[4] U. Kampmann, B. Christensen, T.S. Nielsen, S.B. Pedersen, L. Ørskov, et al., GLUT4 and UBC9 protein expression is reduced in muscle from type 2 diabetic patients with severe insulin resistance, PLoS One 6 (2011) e27854, https://doi.org/10.1371/journal.pone.0027854.

[5] H.G. Joost, G.I. Bell, J.D. Best, M.J. Birnbaum, M.J. Charron, et al., Nomenclature of the GLUT/SLC2A family of sugar/polyol transport facilitators, Am. J. Physiol. Endocrinol. Metab. 282 (2002) E974–E976, https://doi.org/10.1152/ajpendo.00407.2001.

[6] N. Anzai, K. Ichida, P. Jutabha, T. Kimura, E. Babu, et al., Plasma urate level is directly regulated by a voltage-driven urate efflux transporter URATv1 (SLC2A9) in humans, J. Biol. Chem. 283 (2008) 26834–26838, https://doi.org/10.1074/jbc.C800156200.

[7] E. Di Daniel, M.H. Mok, E. Mead, C. Mutinelli, E. Zambello, et al., Evaluation of expression and function of the H+/myo-inositol transporter HMIT, BMC Cell Biol. 10 (2009) 54, https://doi.org/10.1186/1471-2121-10-54.

[8] M. Uldry, M. Ibberson, J.D. Horisberger, J.Y. Chatton, B.M. Riederer, et al., Identification of a mammalian H(+)-*myo*-inositol symporter expressed predominantly in the brain, EMBO J. 20 (2001) 4467–4477, https://doi.org/10.1093/emboj/20.16.4467.

[9] V. Douard, R.P. Ferraris, Regulation of the fructose transporter GLUT5 in health and disease, Am. J. Physiol. Endocrinol. Metab. 295 (2008) E227–E237, https://doi.org/10.1152/ajpendo.90245.2008.

[10] C.F. Burant, J. Takeda, E. Brot-Laroche, G.I. Bell, N.O. Davidson, Fructose transporter in human spermatozoa and small intestine is GLUT5, J. Biol. Chem. 267 (1992) 14523–14526.

[11] Q. Li, A. Manolescu, M. Ritzel, S. Yao, M. Slugoski, et al., Cloning and functional characterization of the human GLUT7 isoform SLC2A7 from the small intestine, Am. J. Physiol. Gastrointest. Liver Physiol. 287 (2004) G236–G242, https://doi.org/10.1152/ajpgi.00396.2003.

[12] A. Manolescu, A.M. Salas-Burgos, J. Fischbarg, C.I. Cheeseman, Identification of a hydrophobic residue as a key determinant of fructose transport by the facilitative hexose transporter SLC2A7 (GLUT7), J. Biol. Chem. 280 (2005) 42978–42983, https://doi.org/10.1074/jbc.M508678200.

[13] A.R. Manolescu, R. Augustin, K. Moley, C. Cheeseman, A highly conserved hydrophobic motif in the exofacial vestibule of fructose transporting SLC2A proteins acts as a critical determinant of their substrate selectivity, Mol. Membr. Biol. 24 (2007) 455–463, https://doi.org/10.1080/09687680701298143.

[14] K. Ebert, M. Ludwig, K.E. Geillinger, G.C. Schoberth, J. Essenwanger, et al., Reassessment of GLUT7 and GLUT9 as putative fructose and glucose transporters, J. Membr. Biol. 250 (2017) 171–182, https://doi.org/10.1007/s00232-016-9945-7.

[15] K. Ebert, M. Ewers, I. Bisha, S. Sander, T. Rasputniac, et al., Identification of essential amino acids for glucose transporter 5 (GLUT5)-mediated fructose transport, J. Biol. Chem. 293 (2018) 2115–2124, https://doi.org/10.1074/jbc.RA117.001442.

[16] E.M. Quistgaard, C. Löw, F. Guettou, P. Nordlund, Understanding transport by the major facilitator superfamily (MFS): structures pave the way, Nat. Rev. Mol. Cell Biol. 17 (2016) 123–132, https://doi.org/10.1038/nrm.2015.25.

[17] D. Deng, C. Xu, P. Sun, J. Wu, C. Yan, et al., Crystal structure of the human glucose transporter GLUT1, Nature 510 (2014) 121–125, https://doi.org/10.1038/nature13306.

[18] D. Deng, P. Sun, C. Yan, M. Ke, X. Jiang, et al., Molecular basis of ligand recognition and transport by glucose transporters, Nature 526 (2015) 391–396, https://doi.org/10.1038/nature14655.

[19] N. Nomura, G. Verdon, H.J. Kang, T. Shimamura, Y. Nomura, et al., Structure and mechanism of the mammalian fructose transporter GLUT5, Nature 526 (2015) 397–401, https://doi.org/10.1038/nature14909.

[20] Z. Shen, L. Xu, T. Wu, H. Wang, Q. Wang, et al., Structural basis for urate recognition and apigenin inhibition of human GLUT9, Nat. Commun. 15 (2024) 5039, https://doi.org/10.1038/s41467-024-49420-9.

[21] Y. Yuan, F. Kong, H. Xu, A. Zhu, N. Yan, et al., Cryo-EM structure of human glucose transporter GLUT4, Nat. Commun. 13 (2022) 2671, https://doi.org/10.1038/s41467-022-30235-5.

[22] L. Sun, X. Zeng, C. Yan, X. Sun, X. Gong, et al., Crystal structure of a bacterial homologue of glucose transporters GLUT1-4, Nature 490 (2012) 361–366, https://doi.org/10.1038/nature11524.

[23] S. Hansen, J.C. Stüber, P. Ernst, A. Koch, D. Bojar, et al., Design and applications of a clamp for Green Fluorescent Protein with picomolar affinity, Sci. Rep. 7 (2017) 16292, https://doi.org/10.1038/s41598-017-15711-z.

[24] I.G. Denisov, Y.V. Grinkova, A.A. Lazarides, S.G. Sligar, Directed self-assembly of monodisperse phospholipid bilayer Nanodiscs with controlled size, J. Am. Chem. Soc. 126 (2004) 3477–3487, https://doi.org/10.1021/ja0393574.

[25] S.S. Lee, J.G. Park, E. Jang, S.H. Choi, S. Kim, et al., W546 stacking disruption traps the human porphyrin transporter ABCB6 in an outward-facing transient state, Commun. Biol. 6 (2023) 960, https://doi.org/10.1038/s42003-023-05339-3.

[26] A. Punjani, J.L. Rubinstein, D.J. Fleet, M.A. Brubaker, cryoSPARC: algorithms for rapid unsupervised cryo-EM structure determination, Nat. Methods 14 (2017) 290–296, https://doi.org/10.1038/nmeth.4169.

[27] A. Punjani, H. Zhang, D.J. Fleet, Non-uniform refinement: adaptive regularization improves single-particle cryo-EM reconstruction, Nat. Methods 17 (2020) 1214–1221, https://doi.org/10.1038/s41592-020-00990-8.

[28] J. Jumper, R. Evans, A. Pritzel, T. Green, M. Figurnov, et al., Highly accurate protein structure prediction with AlphaFold, Nature 596 (2021) 583–589, https://doi.org/10.1038/s41586-021-03819-2.

[29] E.F. Pettersen, T.D. Goddard, C.C. Huang, G.S. Couch, D.M. Greenblatt, et al., UCSF Chimera–a visualization system for exploratory research and analysis, J. Comput. Chem. 25 (2004) 1605–1612, https://doi.org/10.1002/jcc.20084.

[30] P.V. Afonine, B.K. Poon, R.J. Read, O.V. Sobolev, T.C. Terwilliger, et al., Real-space refinement in PHENIX for cryo-EM and crystallography, Acta Crystallogr D Struct Biol 74 (2018) 531–544, https://doi.org/10.1107/S2059798318006551.

[31] P. Emsley, K. Cowtan, *Coot*: model-building tools for molecular graphics, Acta Crystallogr D Biol Crystallogr 60 (2004) 2126–2132, https://doi.org/10.1107/S0907444904019158.

[32] C.J. Williams, J.J. Headd, N.W. Moriarty, M.G. Prisant, L.L. Videau, et al., MolProbity: more and better reference data for improved all-atom structure validation, Protein Sci. 27 (2018) 293–315, https://doi.org/10.1002/pro.3330.

[33] N. Wang, X. Jiang, S. Zhang, A. Zhu, Y. Yuan, et al., Structural basis of human monocarboxylate transporter 1 inhibition by anti-cancer drug candidates, Cell 184 (2021) 370–383 e313, https://doi.org/10.1016/j.cell.2020.11.043.

[34] N. Yan, Structural advances for the major facilitator superfamily (MFS) transporters, Trends Biochem. Sci. 38 (2013) 151–159, https://doi.org/10.1016/j.tibs.2013.01.003.

[35] X. Jiang, Y. Yuan, J. Huang, S. Zhang, S. Luo, et al., Structural basis for blocking sugar uptake into the malaria parasite *plasmodium falciparum*, Cell 183 (2020) 258–268 e212, https://doi.org/10.1016/j.cell.2020.08.015.

[36] J.C. Garcia, M. Strube, K. Leingang, K. Keller, M.M. Mueckler, Amino acid substitutions at tryptophan 388 and tryptophan 412 of the HepG2 (Glut1) glucose transporter inhibit transport activity and targeting to the plasma membrane in Xenopus oocytes, J. Biol. Chem. 267 (1992) 7770–7776.

[37] H. Doege, A. Bocianski, A. Scheepers, H. Axer, J. Eckel, et al., Characterization of human glucose transporter (GLUT) 11 (encoded by SLC2A11), a novel sugar-transport facilitator specifically expressed in heart and skeletal muscle, Biochem. J. 359 (2001) 443–449, https://doi.org/10.1042/0264-6021:3590443.

[38] V. Lalioti, S. Vergarajauregui, I.V. Sandoval, Targeting motifs in GLUT4, Mol. Membr. Biol. 18 (2001) 257–264, https://doi.org/10.1080/09687680110090780 (review).

[39] A. Šali, T.L. Blundell, Comparative protein modelling by satisfaction of spatial restraints, J. Mol. Biol. 234 (1993) 779–815, https://doi.org/10.1006/jmbi.1993.1626.

[40] A. Schürmann, H. Doege, H. Ohnimus, V. Monser, A. Buchs, et al., Role of conserved arginine and glutamate residues on the cytosolic surface of glucose transporters for transporter function, Biochemistry 36 (1997) 12897–12902, https://doi.org/10.1021/bi971173c.

[41] D. Deng, N. Yan, GLUT, SGLT, and SWEET: structural and mechanistic investigations of the glucose transporters, Protein Sci. 25 (2016) 546–558, https://doi.org/10.1002/pro.2858.

[42] S. Sauve, J. Williamson, A. Polasa, M. Moradi, Ins and outs of rocker switch mechanism in major facilitator superfamily of transporters, Membranes 13 (2023), https://doi.org/10.3390/membranes13050462.